



**HAL**  
open science

# Syn-Shearing Deformation Mechanisms of Minerals in Partially Molten Metapelites

Dripta Dutta, Santanu Misra, David Mainprice

► **To cite this version:**

Dripta Dutta, Santanu Misra, David Mainprice. Syn-Shearing Deformation Mechanisms of Minerals in Partially Molten Metapelites. *Geophysical Research Letters*, 2021, 48, 10.1029/2021GL094667 . insu-03661281

**HAL Id: insu-03661281**

**<https://insu.hal.science/insu-03661281>**

Submitted on 24 Jun 2022

**HAL** is a multi-disciplinary open access archive for the deposit and dissemination of scientific research documents, whether they are published or not. The documents may come from teaching and research institutions in France or abroad, or from public or private research centers.

L'archive ouverte pluridisciplinaire **HAL**, est destinée au dépôt et à la diffusion de documents scientifiques de niveau recherche, publiés ou non, émanant des établissements d'enseignement et de recherche français ou étrangers, des laboratoires publics ou privés.

Copyright

# Geophysical Research Letters<sup>®</sup>

## RESEARCH LETTER

10.1029/2021GL094667

### Key Points:

- In an HPT torsion experiment ( $\gamma = 15$ ), quartz-muscovite melted partially and produced K-feldspar, ilmenite, biotite, mullite, and cordierite
- Quartz grain size reduced, muscovite was consumed entirely, K-feldspar grains nucleated first while mullite/cordierite nucleated last
- Melt-assisted grain boundary sliding was the dominant deformation mechanism for the reactants and “in-situ” melt-crystallized phases

### Supporting Information:

Supporting Information may be found in the online version of this article.

### Correspondence to:

S. Misra,  
[smisra@iitk.ac.in](mailto:smisra@iitk.ac.in)

### Citation:

Dutta, D., Misra, S., & Mainprice, D. (2021). Syn-shearing deformation mechanisms of minerals in partially molten metapelites. *Geophysical Research Letters*, 48, e2021GL094667. <https://doi.org/10.1029/2021GL094667>

Received 16 AUG 2021

Accepted 28 OCT 2021

### Author Contributions:

**Conceptualization:** Dripta Dutta, Santanu Misra

**Data curation:** Dripta Dutta, Santanu Misra, David Mainprice

**Formal analysis:** Dripta Dutta, Santanu Misra, David Mainprice

**Funding acquisition:** Santanu Misra

**Investigation:** Dripta Dutta, Santanu Misra

**Methodology:** Dripta Dutta, Santanu Misra, David Mainprice

**Project Administration:** Santanu Misra

**Supervision:** Santanu Misra

**Validation:** Dripta Dutta, Santanu Misra, David Mainprice

**Writing – original draft:** Dripta Dutta, Santanu Misra

**Writing – review & editing:** Dripta Dutta, Santanu Misra, David Mainprice

© 2021. American Geophysical Union.  
All Rights Reserved.

## Syn-Shearing Deformation Mechanisms of Minerals in Partially Molten Metapelites

Dripta Dutta<sup>1</sup> , Santanu Misra<sup>1</sup> , and David Mainprice<sup>2</sup>

<sup>1</sup>Department of Earth Sciences, Indian Institute of Technology Kanpur, Kanpur, India, <sup>2</sup>Géosciences Montpellier UMR CNRS 5243, Université de Montpellier, Montpellier, France

**Abstract** We investigated an experimentally sheared ( $\gamma = 15$ ,  $\dot{\gamma} = 3 \times 10^{-4} \text{ s}^{-1}$ , 300 MPa, 750°C) quartz-muscovite aggregate to understand the deformation of parent and new crystals in partially molten rocks. The scanning electron microscope and electron backscatter diffraction analyses along the longitudinal axial section of the cylindrical sample suggest that quartz and muscovite melted partially and later produced K-feldspar, ilmenite, biotite, mullite, and cordierite. Quartz grains became finer, and muscovite was almost entirely consumed in the process. With increasing  $\gamma$ , melt and crystal fractions decreased and increased, respectively. Among the new minerals, K-feldspar grains (highest area fraction and coarsest) nucleated first, whereas cordierite and mullite grains, finest and least in number, respectively, nucleated last. Fine grain size, weak crystallographic preferred orientations, low intragranular deformation, and equant shapes suggest both initial and new minerals deformed dominantly by melt-assisted grain boundary sliding, which is further substantiated by higher misorientations between adjacent grains of quartz, K-feldspar, and ilmenite.

**Plain Language Summary** The processes governing the deformation of minerals in partially molten rocks are poorly understood as we generally only see the end product. To focus light on this, we sheared quartz and muscovite aggregate to a large shear strain at high pressure and temperature, where these two minerals underwent partial melting and produced new minerals. Electron backscatter diffraction based microstructural investigations of an experimentally sheared partial melt reveal that even at elevated pressure and temperatures, and significant magnitude of deformation, the presence of melt, together with strain partitioning and low intergranular stress transfer, inhibited intragranular plastic deformation in the remaining starting materials and the newly grown crystals.

## 1. Introduction

The deformation behaviors of the dominant minerals, bulk rheologies and overall strength of the lower crustal rocks have been widely investigated (e.g., Incel et al., 2019; Kirby, 1985; Rosenberg & Handy, 2005). However, the accessory minerals, which are often finer in size, are significant in localizing strain (Linckens et al., 2015). Syn-deformational phase nucleation/mixing can also trigger deformation partitioning (Mansard et al., 2018). The growth of the new minerals and their participation in the overall deformation of the rock-suite can happen in solid-state, however, new minerals can also nucleate and grow in the discrete connected melt pockets in a deforming partially molten rock-mass (Lee et al., 2020; Wilson, 1994).

Solid rocks, subjected to deformation at changing P-T-fluid conditions or gain/loss of components of the system can experience changes in phase and melt fraction that affect their deformation, localization, overall mechanical behavior and physical properties (Brown, 1994, 2007; Burg & Vigneresse, 2002; Misra et al., 2014; Soustelle et al., 2014). Several laboratory experiments have been performed to understand the strength and rheology of partially molten rocks (Holyoke & Tullis, 2006; Misra et al., 2011, 2014; Rosenberg, 2001; Turmarkina et al., 2011; van der Molen & Paterson, 1979), and the role of stress in melt distribution and the associated strain partitioning (Holtzman & Kohlstedt, 2007; Holtzman et al., 2003). Laboratory experiments (e.g., Holtzman et al., 2012; Misra et al., 2014), numerical models (e.g., Kaislaniemi et al., 2018), and natural observations (e.g., Davidson et al., 1994; Dijkstra et al., 2002), confirm melt-induced weakening of the host rocks. Previous studies also suggest that the dominant deformation mechanism switches from dislocation creep at low melt fractions (1%–4%) to grain boundary sliding (GBS) once the melt fraction exceeds 7% (Cooper & Kohlstedt, 1984; Hasalová et al., 2008; Walte et al., 2005). However, as the initial deformation

features are generally overprinted by later textural evolution of the rocks, deformation mechanisms of the phases crystallizing “in-situ” in the deforming partially molten rocks are still unknown.

The existing deformation models of partially molten rocks, mostly derived from studying migmatites, illustrate that (a) both melt and melt-crystallized phases are strained during the syn-melting and late-stage solid state deformation, respectively (Prakash et al., 2018); (b) dislocation creep accommodates strain during both pre- and post-melt conditions, but dissolution-precipitation and rigid body rotation dominate under melt-present deformation (Shao et al., 2021); (c) in-situ coarsening is followed by dislocation creep of grains nucleating from the melt (Lee et al., 2020); (d) fine grain size and water saturated conditions favor diffusion creep (Dell'Angelo & Olgaard, 1995; Kilian et al., 2011), whereas presence of melt favors GBS (Lee et al., 2018; Stuart et al., 2018); and (e) the minerals crystallized from the melt may deform by dislocation creep (Miranda & Klepeis, 2016). Crystallographic preferred orientations (CPOs) are generally developed during dislocation creep and therefore provide constrains on the predominant deformation mechanisms. But the CPOs cannot always be the sole proxy for the deformation mechanisms operative during partial melting and subsequent crystallization of the new phases. Instead, the information related to the availability of water/melt or lack thereof should also be considered, which can influence both intra- and intergrain misorientations of the parent and new crystals (Wheeler et al., 2001) during deformation.

In this contribution, we investigated a sample deformed under torsion using scanning electron microscope (SEM) and electron backscatter diffraction (EBSD)-based microtextural analyses to focus on the deformation behavior of both initially present and “in-situ” crystallized (derived from the partial melt) phases in a metapelitic assemblage, analogous to the lower crust, with increasing shear strain.

## 2. Materials and Methods

For this study, we have revisited the deformed sample P1095 of Misra et al. (2011). The initial composition of the sample consisted of a dry homogeneous mixture of quartz (mean grain size: 4.07  $\mu\text{m}$ ) and muscovite (mean grain size: 37.92  $\mu\text{m}$ ,  $(\text{K}_{0.9}\text{Na}_{0.1})(\text{Al}_{1.6}\text{Fe}_{0.3}\text{Mg}_{0.1})[\text{Si}_{3.2}\text{Al}_{0.8}\text{O}_{10}](\text{OH})_2$ ) powders. The ratio (by volume) of quartz to muscovite in the mixture was 7:3. To fabricate a synthetic rock sample, the powder mixture was first cold pressed uniaxially, inside a steel canister of 50 mm diameter, at 200 MPa and then the canister (sealed) was isostatically hot pressed (HIP) for 24 hr at 160 MPa and 580°C. The process of cold press and HIP turned the powder to a dense solid. A cylindrical core of 10 mm diameter (Figure 1a) was drilled from the HIPped canister and then machined to a perfect, 8.04 mm long cylinder. The cylindrical sample was deformed under torsion to a finite shear strain ( $\gamma$ ) of 15 in an internally heated, gas medium deformation apparatus equipped with torsion actuator and internal load cell (Paterson & Olgaard, 2000). The torsion experiment was conducted at 300 MPa confining pressure and 750°C temperature, such that the effective shear strain rate ( $\dot{\gamma}$ ) at the outer annulus of the sample was  $3 \times 10^{-4} \text{ s}^{-1}$ .

The deformed sample was cut and then polished with colloidal quartz along a plane, longitudinal axial (LA) section, which contains the torsion axis (Figure 1a). This polished surface was studied using an SEM equipped with energy dispersive X-ray spectroscopy (EDS) and an EBSD detector. According to the torsion geometry, the mid-line (i.e., the torsion axis) of the sample has zero  $\gamma$  and  $\dot{\gamma}$ , both of which increase away from the torsion axis, that is, toward the periphery, where  $\gamma = 15$  and  $\dot{\gamma} = 3 \times 10^{-4} \text{ s}^{-1}$ . The entire sample was at 750°C and 300 MPa throughout the runtime (about 14 hr). This unique LA section is analogous to the YZ plane of the kinematic strain ellipsoid (Ramsay, 1980) and allows to study the influence of strain on texture and mineral reactions.

To present the systematic observations and data on the sequence of melting, crystallization of new minerals and their mutual relationships (details in Text S1, Figure S1 in Supporting Information S1), we have considered the experimental data of samples deformed at incremental strains (Misra et al., 2014). The relative proportions (area fractions) of the phases were determined from the SEM images (details in Text S2 in Supporting Information S1) and from the EBSD derived phase maps (details in Text S3 in Supporting Information S1).

The post-processing of the EBSD data (details in Text S3 in Supporting Information S1) was performed using MTEX toolbox v5.6.0 (Bachmann et al., 2011; Hielscher & Schaeben, 2008). A threshold angle of 10° was

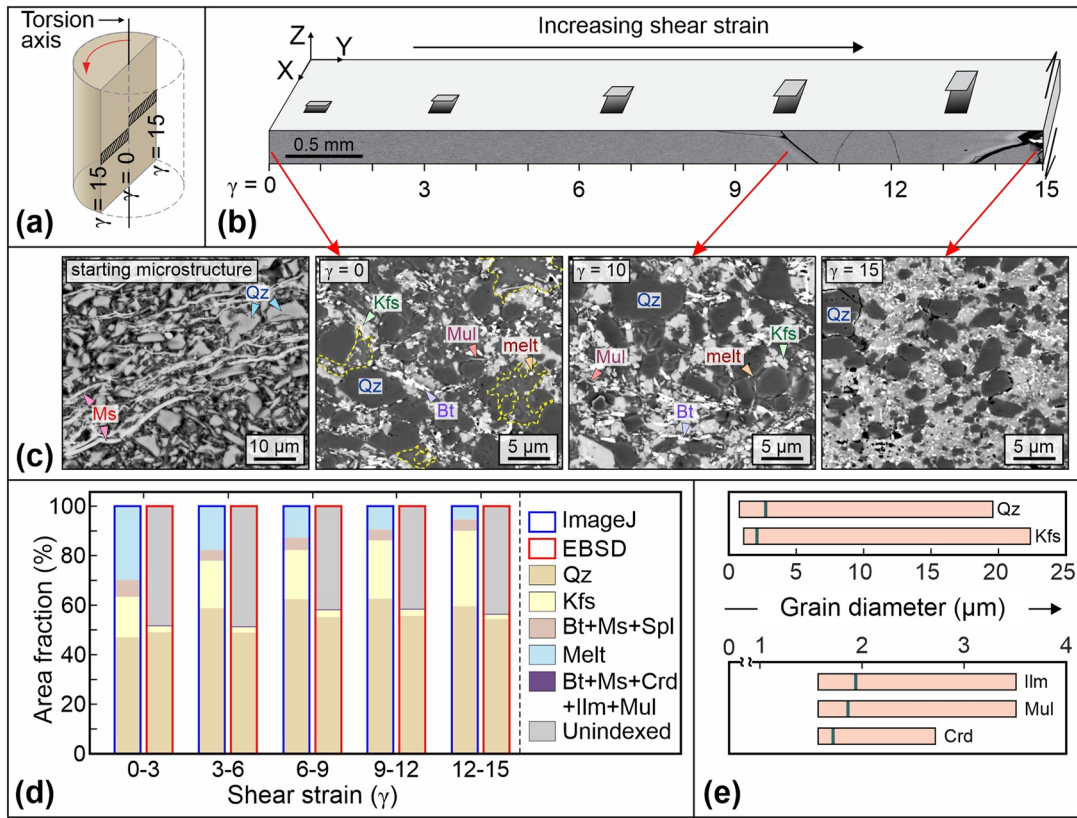


**Figure 1.** (a) Longitudinal axial section of a deformed sample under torsion. The black striped zones are from where EBSD data were obtained. (b) Diagram shows a stripped zone with the standard shear kinematic reference axes (XYZ). (c) SEM images from the LA sections show the distributions of phases in the starting material, melt-patches, and new minerals with increasing  $\gamma$ . (d) Stacked histogram plot showing the area fractions of the different phases, melt and unindexed pixels with increasing  $\gamma$ . (e) Range of grain equivalent diameters of the different phases, except for biotite and muscovite that have <40 grains (see Table S1 in Supporting Information S1). The green vertical bars indicate the respective  $\text{RMS}_{\text{GS}}$  values. Mineral abbreviations are as per (Whitney & Evans, 2010).

selected during grain reconstruction, followed by grain size analysis. Pole figures are plotted using a *one-point-per-grain* model as equal-area, lower hemisphere projections (Figure 2). The center and the horizontal diameter of the projection circle represent the direction (X-SD) and plane (XY-SP) of shearing, respectively (Figure 2a). The density contouring was restricted to pole figures with  $\geq 30$  data points, and scattered pole figure plots are used otherwise. J-index ( $J_{\text{ODF}}$ ) (Bunge, 1981) was calculated for each phase and strain increment using all the indexed points. Misorientation analysis was performed only for phases with  $\geq 30$  grains in a particular strain segment. Axes corresponding to low- ( $2\text{--}10^\circ$ ) and high-angle ( $>40^\circ$ ) misorientations were plotted as inverse pole figures (IPFs) for each phase and contoured if the number was  $\geq 15$ . Quartz grains were merged across the Dauphiné Twin boundaries before this to avoid clustering of the high-angle axes near the [c] axes of the IPFs and highlight the distribution of misorientation axes corresponding to angles other than  $60 \pm 5^\circ$ . The EBSD data were also utilized for computing the equivalent diameter (GS), misorientation to mean (mis2mean), grain orientation spread (GOS) and aspect ratios (R) of the grains (details in Text S3 in Supporting Information S1). The root mean square values of GS, GOS, and R have also been calculated and are referred to as  $\text{RMS}_{\text{GS}}$ ,  $\text{RMS}_{\text{GOS}}$ , and  $\text{RMS}_{\text{R}}$ , respectively.

### 3. Results

The SEM images from the LA section (Figure 1c) show that the sample initially underwent partial melting, and later, phases like K-feldspar, sillimanite/mullite, biotite, and spinel grew as reaction products from the melt and all the muscovite grains were consumed (see Text S1 in Supporting Information S1, also Misra et al., 2011, 2014). Quartz grains remain as isolated, rounded clasts. Melt is seen as patches of various shapes between the quartz grains, largely replacing the muscovite grains. The new euhedral grains grew

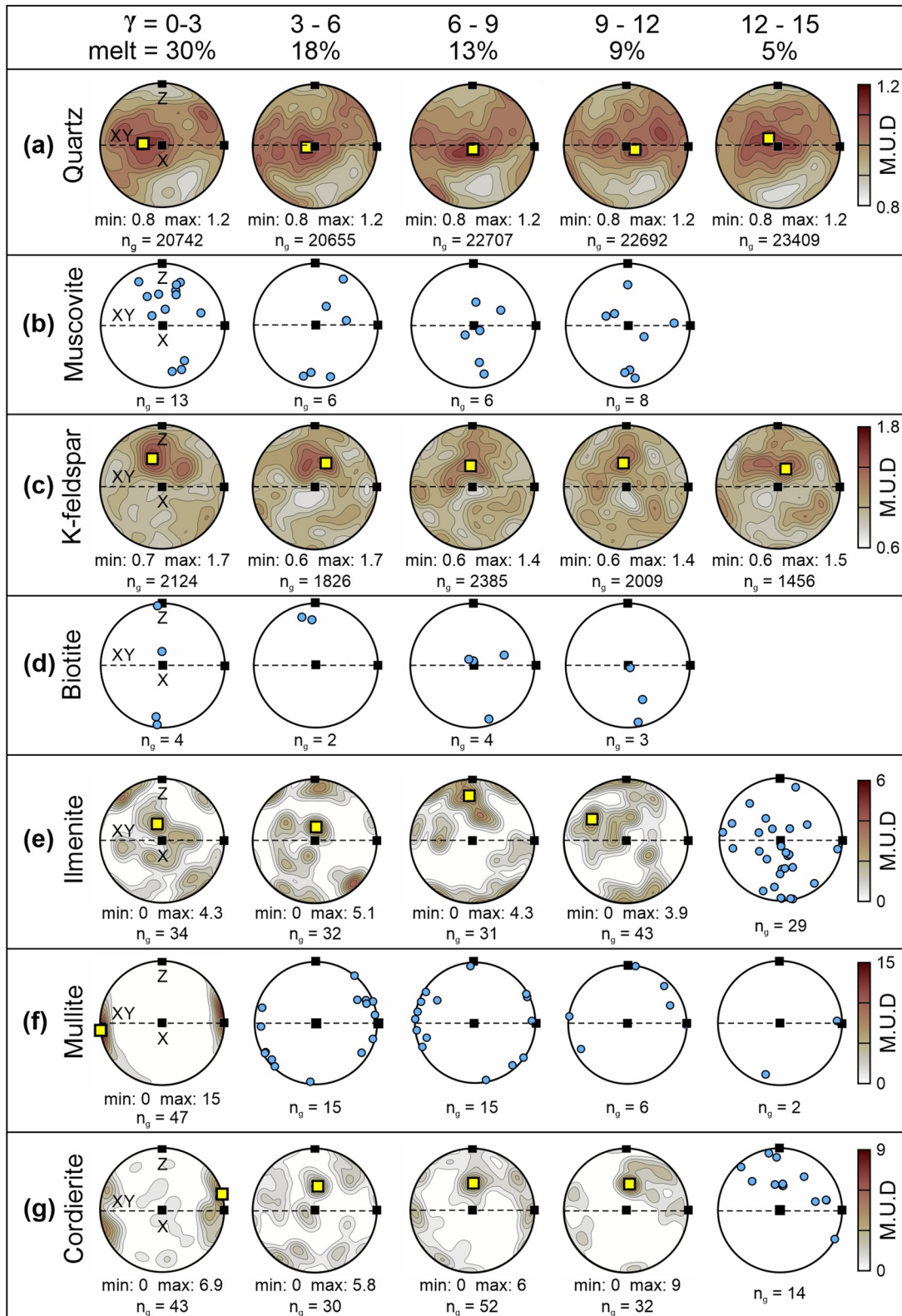


**Figure 2.** [001] pole figures at different strain segments and melt %. The yellow squares denote points of maximum intensity. The reference frame for all the pole figures is illustrated in the first column. The black squares at the center and at the top refer to the X- and Z-axes, respectively, of the kinematic strain ellipsoid. Scattered pole figure plots are shown for  $n_g < 30$ . No grains were detected for muscovite and biotite in the region corresponding to  $\gamma = 12-15$ .  $n_g$  = number of grains. Multiples of uniform density (m.u.d). Color map after Crameri (2018).

mostly within the melt patches with distinct grain boundaries, particularly the large K-feldspars. At the edge of the sample, the melt has largely crystallized. A semi-quantitative image analysis (see Text S2 in Supporting Information S1) of the relative proportions (area%) of the phases from the SEM images shows that the proportion of quartz grains varies from 48% to 64% along the observed sections. The melt proportion is maximum (30%–40%) at the center ( $\gamma = 0$ –1) of the sample (Figure 1d) and gradually decreases toward the edge (2%–3% at  $\gamma = 15$ ). Among the reaction products, the K-feldspar proportions increase from the center to the edge, whereas all other phases, which could not be measured separately, remain equal in proportion (5%–7%; Figure 1d) all along. The EBSD data from the same sample reveal that the reaction products consist of K-feldspar, mullite, cordierite, ilmenite, and biotite. The K-feldspars grew to about 20  $\mu\text{m}$ , maximum, whereas most of the ilmenite, mullite and cordierite grains are in the range of 1.5–3.5  $\mu\text{m}$  (Figure 1e). The difference in the phase identification between SEM-EDS and EBSD could have resulted due to: (a) difficulties detecting <1 wt.% and smaller grain size of cordierite in the sample by EDS analysis (Parian et al., 2015), and (b) the absence of spinel grains within the strip scanned using EBSD. The EBSD-derived phase maps reveal that the spatial distribution of quartz is similar to what has been analyzed from the SEM images (Figure 1d), but that of the K-feldspar is significantly less (8–10 times) in case of the former. The area percentage of K-feldspar grains also does not vary substantially from the center to the edge of the sample. The other reaction products (biotite, ilmenite, mullite, and cordierite) occupy <1% throughout. The low count of these minerals under EBSD, compared to what has been observed in SEM images, is probably due to their smaller grain sizes, which were not always indexed during the EBSD scan. This also justifies a large proportion of unindexed pixels (Figure 1d). In fact, the grains of all the newly crystallized phases are finer than those of quartz (range: 0.8–19  $\mu\text{m}$ ;  $\text{RMS}_{\text{GS}} \sim 3 \mu\text{m}$ ), with those of K-feldspar being the coarsest (range: 1–23  $\mu\text{m}$ ;  $\text{RMS}_{\text{GS}} \sim 2.1 \mu\text{m}$ ). The grains of the rest of the phases are finer ( $\text{RMS}_{\text{GS}} < 2 \mu\text{m}$ ) (Figure 1e) than both quartz and K-feldspar.

The CPO data are viewed in five segments with respect to the strain increments. The quartz [c]-axes maxima lie near the center, that is, parallel to the SD (Figure 2a), possibly implying the dominance of {m}[c] slip system, which is expected at the experimental temperature. There are fewer muscovite grains (<20) but their [001] axes are parallel to the XZ-plane (Figure 2b). The [c]-axes maxima in the K-feldspar pole figures are nearly parallel to the SD for all values of  $\gamma$  (Figure 2c). The distribution of biotite [001] axes is like muscovite (Figure 2d), whereas those of ilmenite are nearly parallel to the SD at  $\gamma < 6$ . [001] axes of the mullite grains exhibit a peripheral distribution with the majority being parallel to the SP but perpendicular to the SD up to  $\gamma < 9$  (Figure 2f). The [c]-axes maxima for cordierite are parallel and oblique to the shear plane at  $\gamma < 3$  and  $\gamma > 3$ , respectively.

$J_{\text{ODF}}$  of quartz and cordierite decrease initially and then rise with increasing  $\gamma$  (Figure S2 in Supporting Information S1). However, the number of indexed points of quartz is high (>29,000) and variation is low (<0.04). Cordierite has <300 indexed points and variation is larger ( $\sim 6 < J_{\text{ODF}} < 23$ ).  $J_{\text{ODF}}$  of K-feldspar increases from  $\sim 1.4$  at  $\gamma < 3$  to  $\sim 2$  at  $\gamma \approx 7$  and then drops to  $\sim 1.5$  at higher  $\gamma$  (Figure S2 in Supporting Information S1).

Low-angle (2–10°) misorientation axes (LAXs) in quartz are either parallel or at high angles to the [0001] axes (Figure 3a), suggesting  $\langle a \rangle$  was the dominant slip direction. Surprisingly, the number of LAXs falls with increasing  $\gamma$ . The high-angle (>40°) misorientation axes (HAXs) are near-perpendicular to the {m} planes for all values of  $\gamma$ . However, for K-feldspar (Figure 3b), the LAXs and HAXs increase up to  $\gamma = 7$  and drop at higher  $\gamma$ . The majority of the LAXs for K-feldspar grains are oblique to [010] except for  $\gamma = 4$  and 15, where they are parallel to [010]. The HAXs are always perpendicular to [010] and are parallel either to the [001] or [100]. The LAXs and HAXs are <15 for all other phases and do not exhibit any distinctive trends (Figures 3c–3e), except the LAXs of mullite and cordierite, which are orthogonal to the [0 0 1]. Biotite and muscovite do not show any misorientation axes. Both the “neighbor-” and “random-pair” misorientation angle distributions (MADs) are near similar for quartz (Figure 4a) and match that of the “theoretical” at all  $\gamma$ . The “random-pair” MADs for K-feldspar (Figure 4b) and ilmenite (Figure 4c) also follow their respective “theoretical” curves for all  $\gamma$  but differ for mullite (Figure 4d) and cordierite (Figure 4e). The frequency of correlated boundaries of all phases is higher than their uncorrelated counterparts for <30°. The mis2mean and GOS values of the entire strip ( $\gamma = 0$ –15), including all phases, do not exceed 10° and 5°, respectively (Figure S3 in Supporting Information S1). The GOS values for the majority of the grains of each of the phases lie in the range 0–0.5° (Figure S4 in Supporting Information S1).

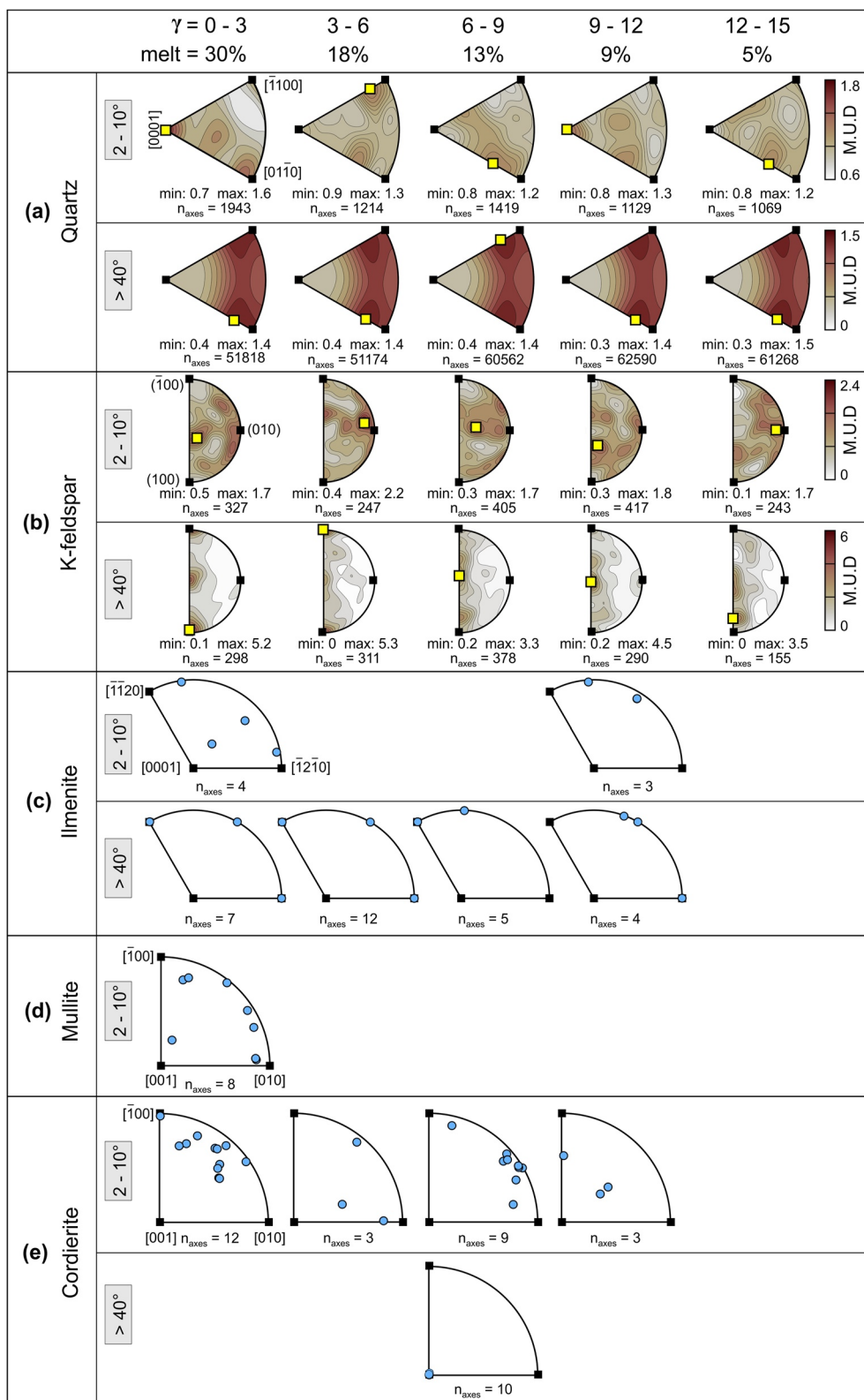


**Figure 3.** Inverse pole figure (IPF) plots of the misorientation axes (both LAXs and HAXs). IPFs in (a) and (b) are contoured to multiples of uniform density (m.u.d) if  $n_{\text{axes}} > 15$ . The distributions are not derived for phases with fewer <30 grains in the respective strain segment.  $n_{\text{axes}}$  = no. of axes. Color map after Crameri (2018).

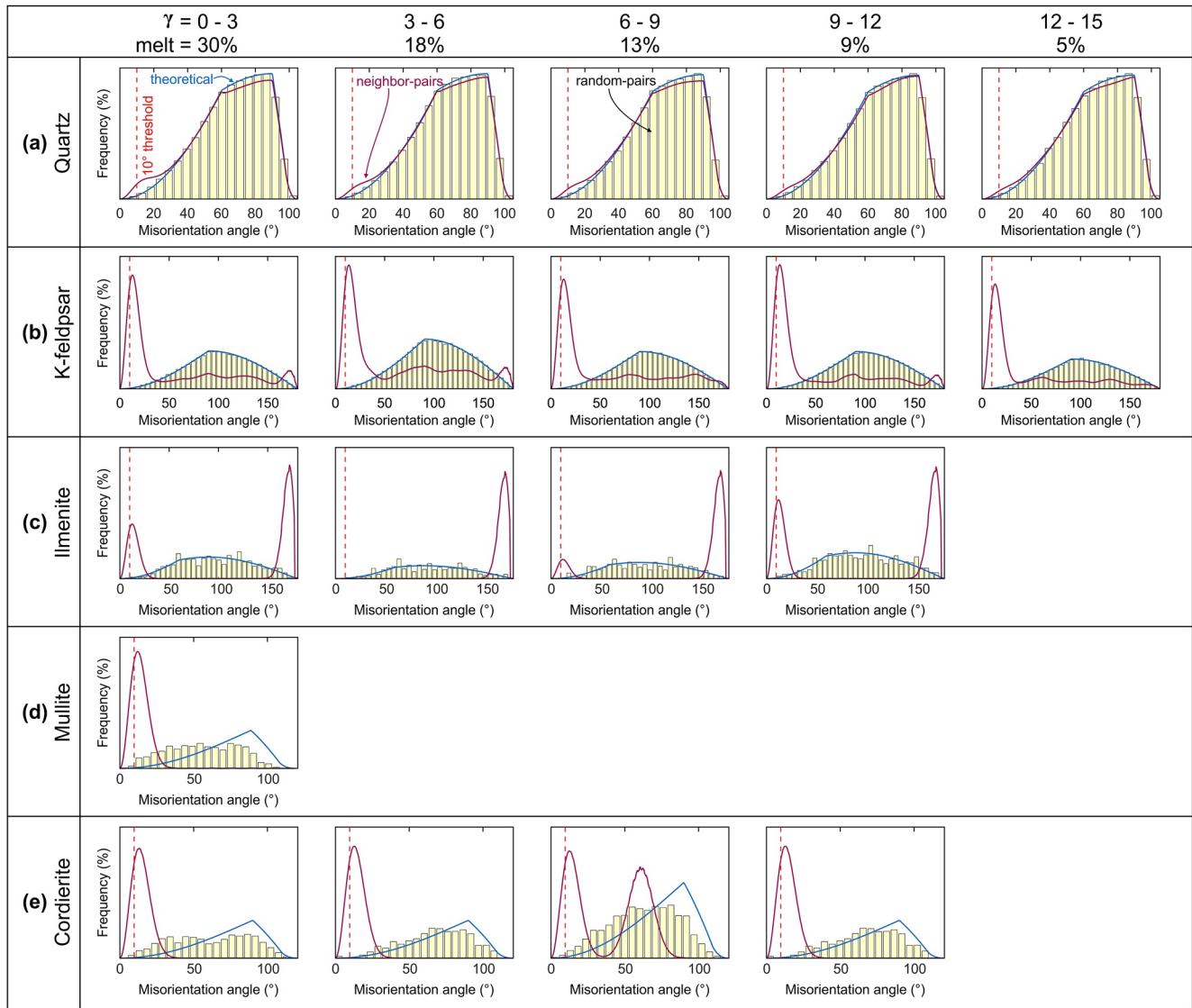


**Figure 4.** Misorientation angle distributions (MADs) of the phases at different shear strain segments and melt percentages. No MADs are shown for phases with <30 grains in the respective strain segment.

The  $RMS_R$  of the quartz, K-feldspar, and cordierite increases with  $\gamma$ , whereas ilmenite exhibits a zig-zag pattern and they lie  $1.4 < RMS_R < 1.5$  (Figure S5 in Supporting Information S1). The other phases have <30 grains in four (mullite) or more (biotite and muscovite) strain segments, and consequently, their variations with strain have not been plotted, as they are statistically insignificant. However, the  $RMS_R$  of biotite, mullite, and muscovite are 1.9, 1.9 and 1.5, respectively. The majority of the quartz, K-feldspar, cordierite grains have aspect ratios <1.5, whereas those of biotite, ilmenite, mullite, and muscovite grains are >1.5.

#### 4. Discussion

The results of microtextural analysis of the deformed and partially molten metapelite provide significant insights into the growth and deformation mechanisms of the melt-derived phases that crystallized “in-situ” during the torsional experiment. It is observed that most of the grains of all the phases have are fine in size ( $RMS_{GS} < 3 \mu m$ , Table S1 in Supporting Information S1). The post-torsion, mean grain size of quartz (2.69  $\mu m$ ) is lower than it was at the beginning (4.07  $\mu m$ ) indicating participation in the reaction process during deformation. Muscovite grains have almost been completely consumed. The initial aggregate first

underwent partial melting followed by nucleation of K-feldspar and then simultaneous nucleation of ilmenite, mullite, biotite, and cordierite (see Text S1 in Supporting Information S1). K-feldspar grains were probably the first to crystallize and grew faster and larger due to the continuous supply of constituent elements from and through the abundant surrounding melt. The finer grain size and smaller numbers of the late-crystallized grains compared to K-feldspar (Figure 1e), could be due to their low crystallization/growth rates at high  $\dot{\gamma}$  (Jurewicz & Watson, 1985) or shear-thinning of the melt-rich zones because of shearing that retarded the growth of ilmenite, mullite, and cordierite (Lee et al., 2018). Mullite and cordierite grains are less common (Figure 2f) and have finer grain sizes (Figure 1e), suggesting that they crystallized later.

Quartz grains exhibit weak CPOs at all  $\gamma$ , possibly implying absence of intracrystalline dislocation creep and/or activation of GBS. The CPOs for K-feldspar grains are also weak and indicate lack of undergone intra-crystalline deformation. We suggest that the thin melt films, present along the boundaries of quartz and K-feldspar grains, absorbed most of the strain and inhibited the solid-state crystal plastic deformation of the grains (Stuart et al., 2018). K-feldspar CPOs are also the weakest among the melt-crystallized phases. This further supports the inference that K-feldspar were the first phase to crystallize but stayed relatively undeformed as the strain was largely partitioned into the surrounding melt. Similar observations have been reported from the migmatites of the Aravalli-Delhi Fold Belt (India; Prakash et al., 2018) and Western Gneiss Region (Norway; Lee et al., 2018), where quartz grains display weak CPOs due to the strain partitioning into weaker melt pools. Ilmenite and cordierite grains, in the studied sample, exhibit CPOs stronger than that of quartz and K-feldspar. We suspect that this could be a consequence of the fewer numbers of grains (<60) that have been detected for both ilmenite and cordierite.

Since CPO data cannot always be reliable indicators of the active deformation mechanisms (Fliervoet et al., 1999; Jiang et al., 2000), we also performed misorientation analysis. Quartz grains host considerable number (>1,000) of low-angle (2–10°) boundaries at all  $\gamma$ , implying dislocation creep. However, the low maximum densities of the LAXs for quartz (Figure 3a) indicate weak correlation between the LAXs and the crystallographic axes, which is further substantiated by the weak misfit between the “neighbor-pair” and theoretical MADs (Figure 4a). Both these observations imply minimum intracrystalline deformation in quartz (Díaz Aspiroz et al., 2007). Higher frequencies of HAXs compared to the LAXs (Figure 3a) favor GBS to be the dominant mechanism instead (Jiang et al., 2000).

K-feldspar LAXs exhibit a weak preferred orientation in the crystal coordinate system (Figure 3b), but, unlike quartz the differences in the number of LAXs and HAXs for each set of the strain increments are lower. The number of LAXs is always lower than the HAXs, when the threshold angle is 10°, instead of 40° (Figure S6 in Supporting Information S1). The identical “random-pair” and “theoretical” MADs (Figure 4b) explains the weak CPO (Figure 2c). Unlike quartz, the misfit between the “neighbor-pair” and “random-pair” MADs of K-feldspar is large, which may have resulted from rotation of the neighboring grains, aided by the presence of melt, to achieve lower interfacial energies (Wheeler et al., 2001). The higher frequency of the “neighbor-pair” MADs than that of the “random-pairs” at lower angles (<50°) also indicates that the adjacent grains must have interacted (Wheeler et al., 2001). On the other hand, similar “random-pair” and “theoretical” MADs for ilmenite imply near random orientation of the grains and further suggest that the relatively strong CPO, compared to quartz and K-feldspar, could be due to fewer grains. Greater misfit between “random-pair” and “theoretical” MADs in mullite and cordierite imply that they are more deformed than ilmenite. In fact, the GOS, for  $\gamma = 0$ –15, also indicates that ilmenite ( $\text{RMS}_{\text{GOS}} = 0.45^\circ$ ) grains are relatively less deformed in comparison to mullite ( $\text{RMS}_{\text{GOS}} = 0.6^\circ$ ) and cordierite ( $\text{RMS}_{\text{GOS}} = 0.8^\circ$ ) grains (Table S1 in Supporting Information S1). The GOS further reveals that all the melt-derived phases are more strained (higher  $\text{RMS}_{\text{GOS}}$  value) than quartz ( $\text{RMS}_{\text{GOS}} = 0.35^\circ$ ), which is one of the starting materials. This observation is not in agreement with that of Shao et al. (2021), wherein the reported *neosomes* (melt-derived phases) are weakly strained than the *residuum* (pre-melt phases). Shao et al. (2021) report that the deformation was partitioned into the melt and consequently the solid phases had weaker CPOs than the minerals strained during pre-melt conditions.

To summarize, fine grain size ( $\text{RMS}_{\text{GS}} < 3 \mu\text{m}$ ), weak CPOs, low internal strains ( $\text{RMS}_{\text{GOS}} < 1.0^\circ$ ), and equant grain shapes ( $\text{RMS}_{\text{R}} < 1.5$ ) suggest GBS was the dominant deformation mechanism (Piazolo & Jaconelli, 2014) affecting both initial and melt-crystallized phases. This deduction is further substantiated by the greater frequencies of HAXs and LAXs for quartz and K-feldspar grains and the presence of >5%

melt fraction throughout ( $\gamma = 0-15$ ). However, deformation processes of muscovite (one of the starting materials) and biotite (melt-crystallized) could not be similarly constrained owing to the relative paucity of grains (<50). Furthermore, considering the number of grains, CPO strengths, and grain sizes, we propose that among the melt-derived phases, K-feldspar was probably the first to crystallize, whereas nucleation of mullite and cordierite began later.

## 5. Conclusions

We experimentally demonstrate, for the first time, the deformation behavior of minerals nucleating and growing in a partially molten environment. The starting quartz-muscovite aggregate underwent grain size reduction (quartz) and was almost consumed (muscovite) to produce partial melts from which K-feldspar, ilmenite, biotite, mullite, and cordierite crystallized. Fine grain sizes, weak CPOs, low intragranular deformation, and equant shapes of the crystals imply deformation by syn-melt grain-boundary sliding. This is also confirmed by the dominance of HAXs over LAXs in quartz, K-feldspar, and ilmenite grains. We further propose that K-feldspar was the first phase that crystallized from the melt, making up the largest volume fraction of product phases, and it is the coarsest of the “in-situ” crystallized phases. Cordierite and mullite grains were perhaps the last to nucleate.

## Data Availability Statement

The EBSD data used in this study can be obtained from the Mendeley Data Repository (<http://dx.doi.org/10.17632/hy9smjhc9n.1>).

## Acknowledgments

We thank A. Kronenberg and an anonymous reviewer for critically reviewing the manuscript and S. Jacobsen for editorial handling. This work is supported by a DST Swarnajayanti Fellowship (DST/SJF/E&ASA-01/2015-16) and an Early Career Research Grant (ECR/2016/001,988), both awarded to SM. DD acknowledges a post-doctoral fellowship from IIT Kanpur.

## References

- Bachmann, F., Hielscher, R., & Schaeben, H. (2011). Grain detection from 2d and 3d EBSD data—Specification of the MTEX algorithm. *Ultramicroscopy*, *111*(12), 1720–1733. <https://doi.org/10.1016/j.ultramic.2011.08.002>
- Brown, M. (1994). The generation, segregation, ascent and emplacement of granite magma: The migmatite-to-crustally-derived granite connection in thickened orogens. *Earth-Science Reviews*, *36*(1), 83–130. [https://doi.org/10.1016/0012-8252\(94\)90009-4](https://doi.org/10.1016/0012-8252(94)90009-4)
- Brown, M. (2007). Crustal melting and melt extraction, ascent and emplacement in orogens: Mechanisms and consequences. *Journal of the Geological Society*, *164*(4), 709–730. <https://doi.org/10.1144/0016-76492006-171>
- Bunge, H. J. (1981). Fabric analysis by orientation distribution functions. *Tectonophysics*, *78*(1–4), 1–21. [https://doi.org/10.1016/0040-1951\(81\)90003-2](https://doi.org/10.1016/0040-1951(81)90003-2)
- Burg, J.-P., & Vigneresse, J.-L. (2002). Non-linear feedback loops in the rheology of cooling-crystallizing felsic magma and heating-melting felsic rock. In S. De Meer, M. R. Drury, J. H. P. De Bresser, & G. M. Pennock (Eds.), *Deformation Mechanisms, Rheology and Tectonics: Current Status and Future Perspectives* (Vol. 200, pp. 275–292). Geological Society. <https://doi.org/10.1144/gsl.sp.2001.200.01.16>. Retrieved from <https://sp.lyellcollection.org/content/200/1/275>
- Cooper, R. F., & Kohlstedt, D. L. (1984). Solution-precipitation enhanced diffusional creep of partially molten olivine-basalt aggregates during hot-pressing. *Tectonophysics*, *107*(3–4), 207–233. [https://doi.org/10.1016/0040-1951\(84\)90252-X](https://doi.org/10.1016/0040-1951(84)90252-X)
- Crameri, F. (2018). *Scientific colour maps (Version 7.0.0)*. Zenodo. <https://doi.org/10.5281/ZENODO.1243862>
- Davidson, C., Schmid, S. M., & Hollister, L. S. (1994). Role of melt during deformation in the deep crust. *Terra Nova*, *6*(2), 133–142. <https://doi.org/10.1111/j.1365-3121.1994.tb00646.x>
- Dell'Angelo, L. N., & Olgaard, D. L. (1995). Experimental deformation of fine-grained anhydrite: Evidence for dislocation and diffusion creep. *Journal of Geophysical Research*, *100*(B8), 15425–15440. <https://doi.org/10.1029/95JB00956>
- Díaz Aspiroz, M., Lloyd, G. E., & Fernández, C. (2007). Development of lattice preferred orientation in clinoamphiboles deformed under low-pressure metamorphic conditions. A SEM/EBSD study of metabasites from the Aracena metamorphic belt (SW Spain). *Journal of Structural Geology*, *29*(4), 629–645. <https://doi.org/10.1016/j.jsg.2006.10.010>
- Dijkstra, A. H., Drury, M. R., & Frijhoff, R. M. (2002). Microstructures and lattice fabrics in the Hilti mantle section (Oman Ophiolite): Evidence for shear localization and melt weakening in the crust-mantle transition zone?: Microstructures and lattice fabrics. ETG 2-1-ETG 2-18. *Journal of Geophysical Research*, *107*(B11), 2–1. <https://doi.org/10.1029/2001JB000458>
- Fliervoet, T. F., Drury, M. R., & Chopra, P. N. (1999). Crystallographic preferred orientations and misorientations in some olivine rocks deformed by diffusion or dislocation creep. *Tectonophysics*, *303*(1), 1–27. [https://doi.org/10.1016/S0040-1951\(98\)00250-9](https://doi.org/10.1016/S0040-1951(98)00250-9)
- Hasalová, P., Schulmann, K., Lexa, O., Štípská, P., Hroudá, F., Ulrich, S., et al. (2008). Origin of migmatites by deformation-enhanced melt infiltration of orthogneiss: A new model based on quantitative microstructural analysis. *Journal of Metamorphic Geology*, *26*(1), 29–53. <https://doi.org/10.1111/j.1525-1314.2007.00743.x>
- Hielscher, R., & Schaeben, H. (2008). A novel pole figure inversion method: Specification of the MTEX algorithm. *Journal of Applied Crystallography*, *41*(6), 1024–1037. <https://doi.org/10.1107/S0021889808030112>
- Holtzman, B. K., Groebner, N. J., Zimmerman, M. E., Ginsberg, S. B., & Kohlstedt, D. L. (2003). Stress-driven melt segregation in partially molten rocks. *Geochemistry, Geophysics, Geosystems*, *4*(5), 8607. <https://doi.org/10.1029/2001GC000258>
- Holtzman, B. K., King, D. S. H., & Kohlstedt, D. L. (2012). Effects of stress-driven melt segregation on the viscosity of rocks. *Earth and Planetary Science Letters*, *359*(360), 184–193. <https://doi.org/10.1016/j.epsl.2012.09.030>
- Holtzman, B. K., & Kohlstedt, D. L. (2007). Stress-driven melt segregation and strain partitioning in partially molten rocks: Effects of stress and strain. *Journal of Petrology*, *48*(12), 2379–2406. <https://doi.org/10.1093/ptrology/egm065>

- Holyoke, C. W., & Tullis, J. (2006). The interaction between reaction and deformation: An experimental study using a biotite + plagioclase + quartz gneiss: Reaction and deformation. *Journal of Metamorphic Geology*, 24(8), 743–762. <https://doi.org/10.1111/j.1525-1314.2006.00666.x>
- Incel, S., Labrousse, L., Hilairat, N., John, T., Gasc, J., Shi, F., et al. (2019). Reaction-induced embrittlement of the lower continental crust. *Geology*, 47(3), 235–238. <https://doi.org/10.1130/G45527.1>
- Jiang, Z., Prior, D. J., & Wheeler, J. (2000). Albite crystallographic preferred orientation and grain misorientation distribution in a low-grade mylonite: Implications for granular flow. *Journal of Structural Geology*, 22(11–12), 1663–1674. [https://doi.org/10.1016/S0191-8141\(00\)00079-1](https://doi.org/10.1016/S0191-8141(00)00079-1)
- Jurewicz, S. R., & Watson, E. B. (1985). The distribution of partial melt in a granitic system: The application of liquid phase sintering theory. *Geochimica et Cosmochimica Acta*, 49(5), 1109–1121. [https://doi.org/10.1016/0016-7037\(85\)90002-X](https://doi.org/10.1016/0016-7037(85)90002-X)
- Kaislaniemi, L., Hunen, J., & Bouilhol, P. (2018). Lithosphere destabilization by melt weakening and crust-mantle interactions: Implications for generation of granite-Migmatite belts. *Tectonics*, 37(9), 3102–3116. <https://doi.org/10.1029/2018TC005014>
- Kilian, R., Heilbronner, R., & Stünitz, H. (2011). Quartz grain size reduction in a granitoid rock and the transition from dislocation to diffusion creep. *Journal of Structural Geology*, 33(8), 1265–1284. <https://doi.org/10.1016/j.jsg.2011.05.004>
- Kirby, S. H. (1985). Rock mechanics observations pertinent to the rheology of the continental lithosphere and the localization of strain along shear zones. *Tectonophysics*, 119(1–4), 1–27. [https://doi.org/10.1016/0040-1951\(85\)90030-7](https://doi.org/10.1016/0040-1951(85)90030-7)
- Lee, A. L., Lloyd, G. E., Torvela, T., & Walker, A. M. (2020). Evolution of a shear zone before, during and after melting. *Journal of the Geological Society*, 177(4), 738–751. <https://doi.org/10.1144/jgs2019-114>
- Lee, A. L., Torvela, T., Lloyd, G. E., & Walker, A. M. (2018). Melt organisation and strain partitioning in the lower crust. *Journal of Structural Geology*, 113, 188–199. <https://doi.org/10.1016/j.jsg.2018.05.016>
- Linckens, J., Herwegh, M., & Müntener, O. (2015). Small quantity but large effect — How minor phases control strain localization in upper mantle shear zones. *Tectonophysics*, 643, 26–43. <https://doi.org/10.1016/j.tecto.2014.12.008>
- Mansard, N., Raimbourg, H., Augier, R., Précigout, J., & Le Breton, N. (2018). Large-scale strain localization induced by phase nucleation in mid-crustal granitoids of the south Armorican massif. *Tectonophysics*, 745, 46–65. <https://doi.org/10.1016/j.tecto.2018.07.022>
- Miranda, E. A., & Klepeis, K. A. (2016). The interplay and effects of deformation and crystallized melt on the rheology of the lower continental crust, Fiordland, New Zealand. *Journal of Structural Geology*, 93, 91–105. <https://doi.org/10.1016/j.jsg.2016.09.007>
- Misra, S., Burg, J.-P., & Mainprice, D. (2011). Effect of finite deformation and deformation rate on partial melting and crystallization in metapelites. *Journal of Geophysical Research*, 116(B2), B02205. <https://doi.org/10.1029/2010JB007865>
- Misra, S., Burg, J.-P., Vigneresse, J.-L., & Mainprice, D. (2014). Rheological transition during large strain deformation of melting and crystallizing metapelites. *Journal of Geophysical Research: Solid Earth*, 119(5), 3971–3985. <https://doi.org/10.1002/2013JB010777>
- Parian, M., Lamberg, P., Möckel, R., & Rosenkranz, J. (2015). Analysis of mineral grades for geometallurgy: Combined element-to-mineral conversion and quantitative X-ray diffraction. *Minerals Engineering*, 82, 25–35. <https://doi.org/10.1016/j.mineng.2015.04.023>
- Paterson, M. S., & Olgaard, D. L. (2000). Rock deformation tests to large shear strains in torsion. *Journal of Structural Geology*, 22(9), 1341–1358. [https://doi.org/10.1016/S0191-8141\(00\)00042-0](https://doi.org/10.1016/S0191-8141(00)00042-0)
- Piazolo, S., & Jaconelli, P. (2014). Sillimanite deformation mechanisms within a Grt-Sil-Bt gneiss: Effect of pre-deformation grain orientations and characteristics on mechanism, slip-system activation and rheology. In S. Llana-Funez, A. Marcos, & F. Bastida (Eds.), *Deformation Structures and Processes within the Continental Crust* (Vol. 394, pp. 189–213). Geological Society, Special Publications. <https://doi.org/10.1144/sp394.10>
- Prakash, A., Piazolo, S., Saha, L., Bhattacharya, A., Pal, D. K., & Sarkar, S. (2018). Deformation behavior of migmatites: Insights from microstructural analysis of a garnet–sillimanite–mullite–quartz–feldspar-bearing anatectic migmatite at Rampura–Agucha, Aravalli–Delhi Fold Belt, NW India. *International Journal of Earth Sciences*, 107(6), 2265–2292. <https://doi.org/10.1007/s00531-018-1598-6>
- Ramsay, J. (1980). Shear zone geometry: A review. *Journal of Structural Geology*, 2(1–2), 83–99. [https://doi.org/10.1016/0191-8141\(80\)90038-3](https://doi.org/10.1016/0191-8141(80)90038-3)
- Rosenberg, C. L. (2001). Deformation of partially molten granite: A review and comparison of experimental and natural case studies. *International Journal of Earth Sciences*, 90(1), 60–76. <https://doi.org/10.1007/s005310000164>
- Rosenberg, C. L., & Handy, M. R. (2005). Experimental deformation of partially melted granite revisited: Implications for the continental crust. *Journal of Metamorphic Geology*, 23(1), 19–28. <https://doi.org/10.1111/j.1525-1314.2005.00555.x>
- Shao, Y., Piazolo, S., Liu, Y., Lee, A. L., Jin, W., Li, W., et al. (2021). Deformation behavior and inferred seismic properties of tonalitic migmatites at the time of pre-melting, partial melting, and post-solidification. *Geochemistry, Geophysics, Geosystems*, 22(2), e2020GC009202. <https://doi.org/10.1029/2020GC009202>
- Soustelle, V., Walte, N. P., Manthilake, M. A. G. M., & Frost, D. J. (2014). Melt migration and melt-rock reactions in the deforming Earth's upper mantle: Experiments at high pressure and temperature. *Geology*, 42(1), 83–86. <https://doi.org/10.1130/G34889.1>
- Stuart, C. A., Piazolo, S., & Daczko, N. R. (2018). The recognition of former melt flux through high-strain zones. *Journal of Metamorphic Geology*, 36(8), 1049–1069. <https://doi.org/10.1111/jmg.12427>
- Tumarkina, E., Misra, S., Burlini, L., & Connolly, J. A. D. (2011). An experimental study of the role of shear deformation on partial melting of a synthetic metapelite. *Tectonophysics*, 503(1), 92–99. <https://doi.org/10.1016/j.tecto.2010.12.004>
- van der Molen, I., & Paterson, M. S. (1979). Experimental deformation of partially-melted granite. *Contributions to Mineralogy and Petrology*, 70(3), 299–318. <https://doi.org/10.1007/BF00375359>
- Walte, N. P., Bons, P. D., & Passchier, C. W. (2005). Deformation of melt-bearing systems—Insight from in situ grain-scale analogue experiments. *Journal of Structural Geology*, 27(9), 1666–1679. <https://doi.org/10.1016/j.jsg.2005.05.006>
- Wheeler, J., Prior, D., Jiang, Z., Spiess, R., & Trimby, P. (2001). The petrological significance of misorientations between grains. *Contributions to Mineralogy and Petrology*, 141(1), 109–124. <https://doi.org/10.1007/s004100000225>
- Whitney, D. L., & Evans, B. W. (2010). Abbreviations for names of rock-forming minerals. *American Mineralogist*, 95(1), 185–187. <https://doi.org/10.2138/am.2010.3371>
- Wilson, C. J. L. (1994). Crystal growth during a single-stage opening event and its implications for syntectonic veins. *Journal of Structural Geology*, 16(9), 1283–1296. [https://doi.org/10.1016/0191-8141\(94\)90070-1](https://doi.org/10.1016/0191-8141(94)90070-1)